Table S1.

Inhibitory effect of the inhibitor GKT 136901 on ROS producing enzymes, redox-sensitive enzymes and others proteins.

Figure S1.

MLEC isolation from WT and NOX deficient mice. a. Flow cytometry analysis of endothelial surface molecules on isolated MLEC. PECAM-1, VE-Cadherin, ICAM-2 and Meca-32 expression level in MLEC. b. PECAM-1 immunofluorescence staining of WT, NOX1 KO and NOX4 KO MLEC. Nuclei in blue (DAPI), and PECAM-1 in purple (Cy5). Images were acquired with a 40x/1.3 numeric aperture lens and analyzed using LSM510 Meta microscope (Carl Zeiss).

Figure S2.

Inhibition of NOX-dependent ROS production by GKT136901 and DPI. a. Concentration-response curves of GKT136901 on NOX1 (x), NOX2 ▲), NOX4 (◊) and Xanthine Oxidase (XO) (□). b. Concentration-response curve of DPI on NOX1 (x), NOX2 (▲), NOX4 (◊) and Xanthine Oxidase (XO) (□) Results are from one experiment performed in triplicate, representative of four performed. Values are presented as means ± s.e.m.

Figure S3.

NOX dependant ROS blocking agents efficiently block endothelial cell migration and branching capacities. a. Migration of endothelial cells was analyzed by a wound-healing assay in presence of different inhibitors that block NADPH dependant ROS production. b. Tubular structure formation was measured by 3D culture using the mouse endothelial cell line in presence of different inhibitors that block NADPH dependant ROS production. Results are expressed in % of control ± s.e.m, n = 3.

Figure S4.

NOX1 over-expression enhances endothelial cell migration and tube-like structure formation. a. In vitro migration was analyzed by wound-healing assay using endothelioma cell lines transfected with NOX1 expressing vector. b. Tubular structure formation was measured by 3D culture of endothelioma cell lines transfected with NOX1 expressing vector. Results are expressed in % of control ± s.e.m. *$p < 0.05$ using Student's t-test.

Figure S5.

AKT but ERK 1/2 activation is affected by NOX1 deficiency. NOX1-deficient MLEC does not activate Akt after bFGF stimulation but present no difference in ERK1/2 activation. a. Western blot analysis of Akt phosphorylation in WT and NOX1-deficient MLEC after 10 min stimulation with 20 ng/ml of bFGF. The graph shows the abundance of phosphorylated Akt relative to total Akt ± s.e.m as determined by densitometry. n = 3. b. Western blot analysis of ERK1/2 phosphorylation in WT and NOX1-deficient MLEC stimulated for 10 min with 20 ng/ml of bFGF. The graph shows the abundance of phosphorylated ERK1/2 relative to total ERK1/2 ± s.e.m as determined by densitometry. n = 3.

Figure S6.

NF-κB nuclear translocation is inhibited in the absence of NOX1 and dependent on PPARα activation. VEGF or b-FGF stimulation of endothelial cells induced p65 NF-κB translocation into the nucleus. This nuclear translocation is not observed in NOX1-deficient cells but restored by PPARα antagonist treatment (GW6471). Immunofluorescence, anti-p65 NF-κB of MLEC (a) and endothelioma cell lines (b) stimulated with VEGF or bFGF in presence or absence of GW6471 (10mM). NF-κB in green (Alexa 488), nuclei in blue (DAPI). Scale bar represent 20 mm. Images were acquired with a 40x/1.3 numeric aperture and analyzed using LSM510 confocal microscope (Carl Zeiss).

Figure S7.

Effect of GKT 136901 on tumor cells. a. LLC1 and B16F0 cell proliferation was measured by EdU incorporation and propidium iodide staining of DNA content, 24h after incubation with 10 μM of GKT136901. b. LLC1 apoptosis was measured by AnnexinV/PI staining after 24h of incubation with 10 μM of GKT136901. c. ROS levels produced by LLC1 are inhibited by GKT136901. ROS production was quantified by DHE substrate 1h after incubation with 10 μM of the inhibitor. *** $p<0.001$ (student t-test).

Figure S8.

Non toxic effect GKT 136901 on mice organs. Heart (a), Kidney (b), Liver (c) and Lung (d) of mice treated orally with vehicle or with vehicle plus GKT136901 inhibitor at 40 mg/kg per day during 8 days, stained by Hematoxilin/Eosin. Scale bars represent 100 μm on the full picture and 20 μm on the zoom. Images were acquired with a 20x/0.8 numeric aperture and analyzed using Mirax (Carl Zeiss).

Enzyme	% Inhibition at 10 μM
Xanthine oxidase	5%
iNoS	0%
eNos	6%
cNos	0%
MPO	0%
12-Lipoxygenase	2%
MAO-B	0%
PKC a, bI, bII, d	0%
PI3K a, b, d, g	0%

Table S1.
Inhibitory effect of the inhibitor GKT 136901 on ROS producing enzymes, redox-sensitive enzymes and others proteins.

Figure S1

A

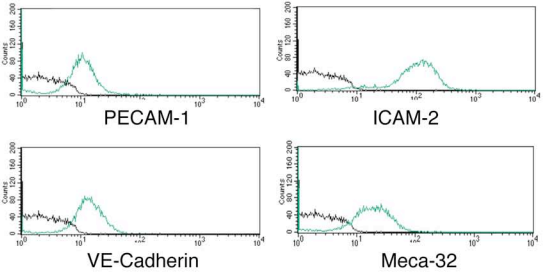

B

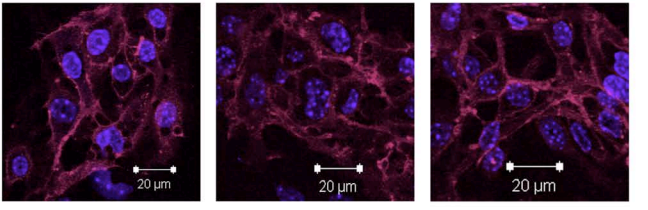

WT **NOX1 KO** **NOX4 KO**

Figure S2

A

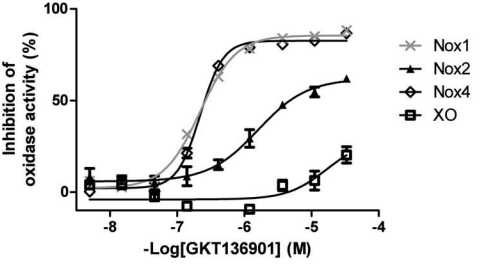
100
50
0
Inhibition of oxidase activity (%)
-8
-7
-6
-5
-4
-Log[GKT136901] (M)
Nox1
Nox2
Nox4
XO

B

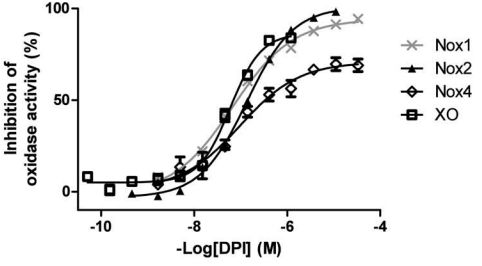
100
50
0
Inhibition of oxidase activity (%)
-10
-8
-6
-4
-Log[DPI] (M)
Nox1
Nox2
Nox4
XO

Figure S3

A

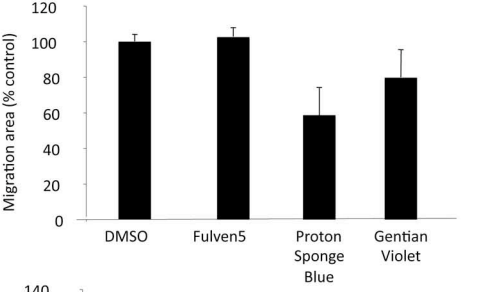
Migration area (% control)
120
100
80
60
40
20
0
DMSO
Fulven5
Proton Sponge Blue
Gentian Violet

B

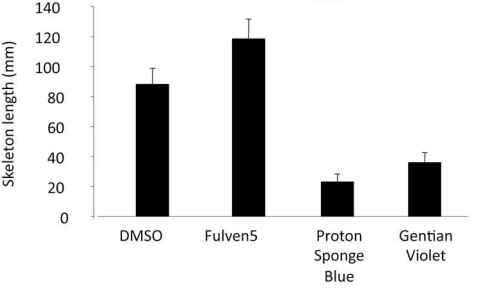
Skeleton length (mm)
140
120
100
80
60
40
20
0
DMSO
Fulven5
Proton Sponge Blue
Gentian Violet

Figure S4

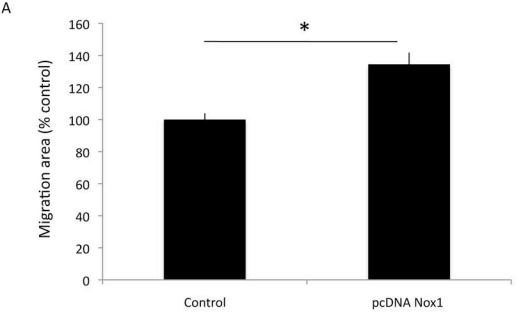
A
*
Migration area (% control)
160
140
120
100
80
60
40
20
0
Control
pcDNA Nox1

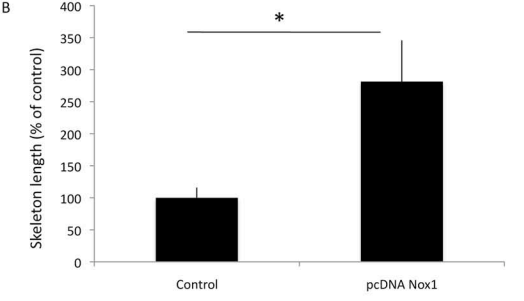
B
*
Skeleton length (% of control)
400
350
300
250
200
150
100
50
0
Control
pcDNA Nox1

Figure S5

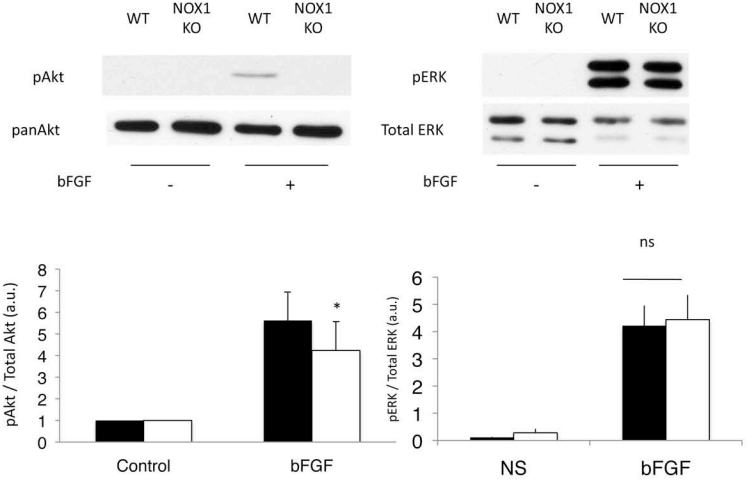
WT
NOX1 KO
WT
NOX1 KO
pAkt
panAkt
bFGF
-
+
WT
NOX1 KO
WT
NOX1 KO
pERK
Total ERK
bFGF
-
+
pAkt / Total Akt (a.u.)
0
1
2
3
4
5
6
7
8
*
Control
bFGF
pERK / Total ERK (a.u.)
0
1
2
3
4
5
6
ns
NS
bFGF

Figure S6

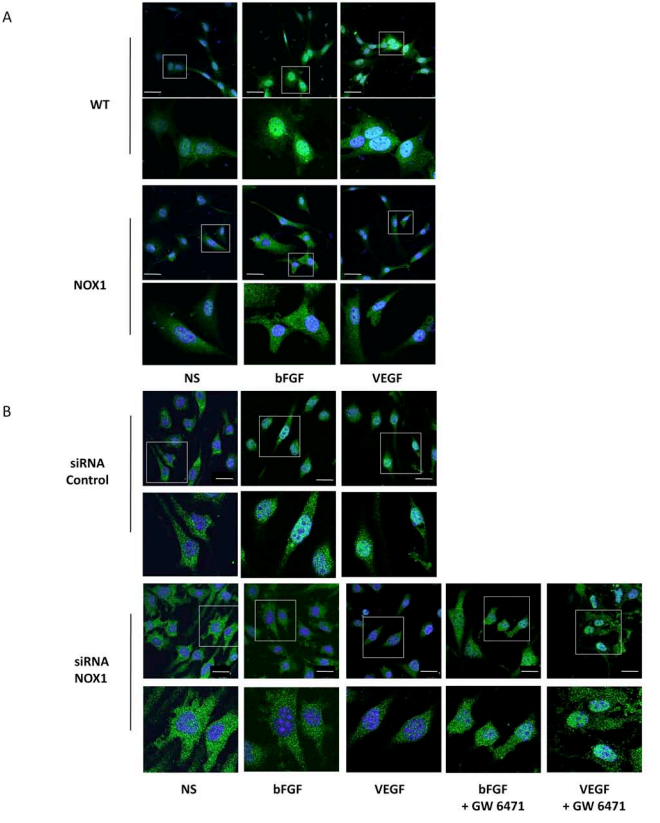
A
WT
NOX1
NS
bFGF
VEGF
B
siRNA
Control
siRNA
NOX1
NS
bFGF
VEGF
bFGF
+ GW 6471
VEGF
+ GW 6471

Figure S7

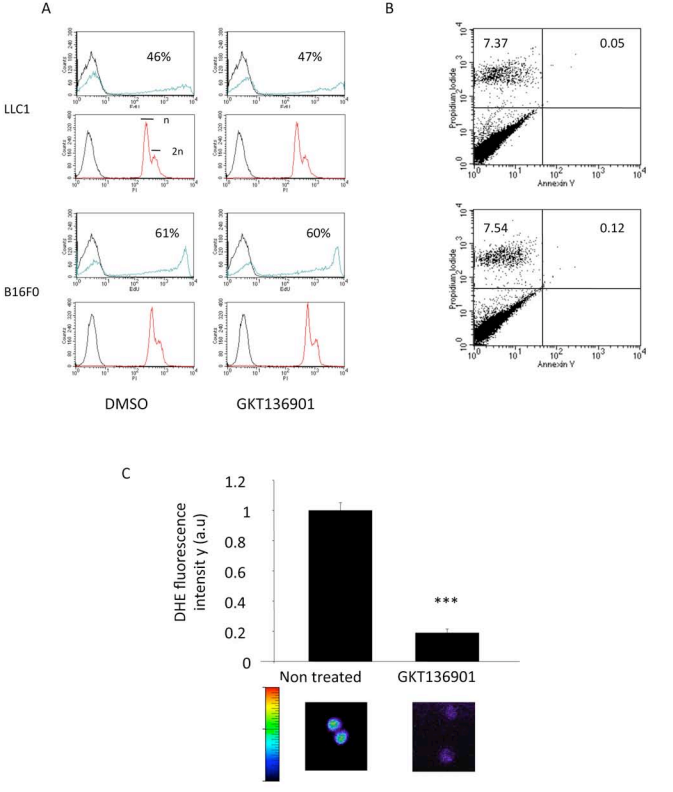
A
B
C
LLC1
B16F0
46%
47%
61%
60%
n
2n
DMSO
GKT136901
7.37
0.05
7.54
0.12
Propidium Iodide
Annexin V
DHE fluorescence intensit y (a.u)
1.2
1
0.8
0.6
0.4
0.2
0
***
Non treated
GKT136901

Figure S8.

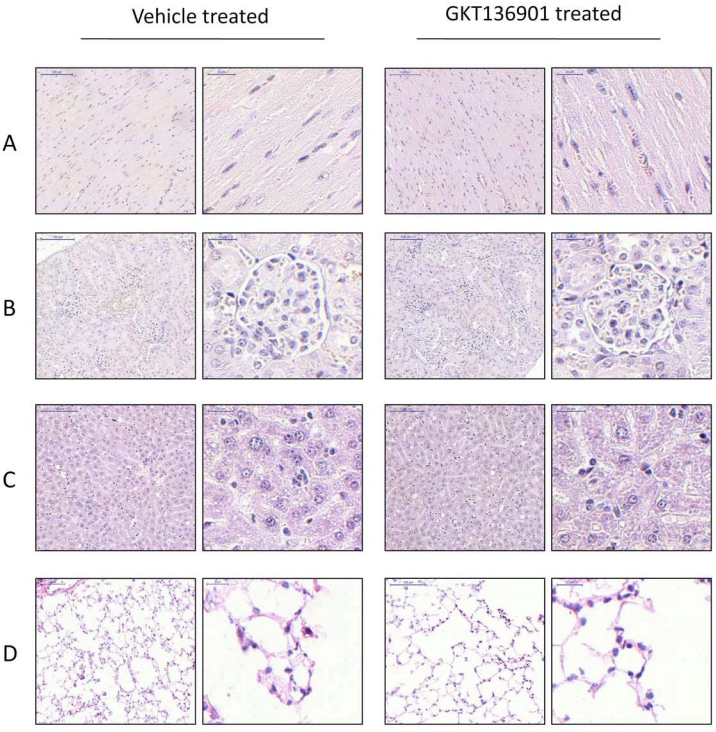

Gene	Primer Forward	Primer Reverse
mu_nox1	CAG TTA TTC ATA TCA TTG CAC ACC TAT TT	CAG AAG CGA GAG ATC CAT CCA
mu_nox2	CAG GAA CCT CAC TTT CCA TAA GAT	AAC GTT GAA GAG ATG TGC AAT TGT
mu_nox4	CCG GAC AGT CCT GGC TTA TCT	TGC TTT TAT CCA ACA ATC TTC TTG TT
mu_ppar-alpha	CCT CAG GGT ACC ACT ACG GAG T	GCC GAA TAG TTC GCC GAA
mu_ppar-gamma	TTC CAC TAT GGA GTT CAT GCT TGT	TCC GGC AGT TAA GAT CAC ACC TA
mu_tubulin	GCA GTG CGG CAA CCA GAT	AGT GGG ATC AAT GCC ATG CT
hu_nox1	GAA GTG GGG CAG TAT ATC TTT GTT A	CTT CTA TCT TGA AAT CCA TCT GGT ACA AAT TC
hu_nox2	TGG AGT GGC ACC CTT TTA CAC,	CCA CAA GCA TTG AAC AGC CC
hu_nox4	CAG GAG GGC TGC TGA AGT ATC AA	TAT CCG GAG CAA TAA GCC AGT CA
hu_b2microglobulin	AAG ATG AGT ATG CCT GCC GTG	CGG CAT CTT CAA ACC TCC AT
mu_VEGF	AGCCGAGCTCATGGACGGGT	TGGCGGGCTCCTCTCCCTTC
mu_FGF2	ATG GCG TCC GCG AGA AGA GC	ACC GGT TGG CAC ACA CTC CC
mu_Catalase	GGACAGTCGGGACCCAGCCA	ATTGGGTTCCCGCCTCCGGT
mu_GPX3	TGGCTGAGCGCTTCGGACAC	AAGGCAGGATGCCCGGAGGA
mu_VCAM-1	CCCGGATCTCAGGTGGCTGC	GCGTGGATTTGGCCCCCTCA
mu-MMP-2	TTGGGCTGCCCCAGACAGGT	GTCCCACTTGGGCTTGCGGG
mu-MMP-9	GGCCGCTCGGATGGTTACCG	TCGCGTCCACTCGGGTAGGG
mu-uPAR	CCA CAG CGA AAA GAC CAA CA	TGT CAG GCT GAT GAT CAT GGA
VE-Cadherin	GGA ACA ACC TTC CAG CTT CAC T	TGA ATA CCT CGT GCG AAA ACA C

Materials and methods S1: Real-time PCR primer sequence list.